catalysts

MDPI

Article

Carbon Nanotube Formation on Cr-Doped Ferrite Catalyst during Water Gas Shift Membrane Reaction: Mechanistic Implications and Extended Studies on Dry Gas Conversions

Xinhui Sun, Antonios Arvanitis, Devaiah Damma, Noe T. Alvarez, Vesselin Shanov, Panagiotis G. Smirniotis and Junhang Dong *

Department of Chemical and Environmental Engineering, University of Cincinnati, Cincinnati, OH 45221, USA; sunxh@mail.uc.edu (X.S.); arvanias@ucmail.uc.edu (A.A.); dammadh@ucmail.uc.edu (D.D.); alvarene@UCMAIL.UC.EDU (N.T.A.); SHANOVVN@UCMAIL.UC.EDU (V.S.); smirnipp@ucmail.uc.edu (P.G.S.)
* Correspondence: junhang.dong@uc.edu

Received: 28 July 2020; Accepted: 10 August 2020; Published: 12 August 2020

Abstract: A nanocrystalline chromium-doped ferrite (FeCr) catalyst was shown to coproduce H_2 and multiwalled carbon nanotubes (MWCNTs) during water gas shift (WGS) reaction in a H_2-permselective zeolite membrane reactor (MR) at reaction pressures of ~20 bar. The FeCr catalyst was further demonstrated in the synthesis of highly crystalline and dimensionally uniform MWCNTs from a dry gas mixture of CO and CH_4, which were the apparent sources for MWCNT growth in the WGS MR. In both the WGS MR and dry gas reactions, the operating temperature was 500 °C, which is significantly lower than those commonly used in MWCNT production by chemical vapor deposition (CVD) method from CO, CH_4, or any other precursor gases. Extensive ex situ characterizations of the reaction products revealed that the FeCr catalyst remained in partially reduced states of Fe^{3+}/Fe^{2+} and Cr^{6+}/Cr^{3+} in WGS membrane reaction while further reduction of Fe^{2+} to Fe^0 occurred in the CO/CH_4 dry gas environments. The formation of the metallic Fe nanoparticles or catalyst surface dramatically improved the crystallinity and dimensional uniformity of the MWCNTs from dry gas reaction as compared to that from WGS reaction in the MR. Reaction of the CO/CH_4 mixture containing 500 ppmv H_2S also resulted in high-quality MWCNTs similar to those from the H_2S-free feed gas, demonstrating excellent sulfur tolerance of the FeCr catalyst that is practically meaningful for utilization of biogas and cheap coal-derived syngas.

Keywords: Cr-doped ferrite; membrane reactor; water gas shift; carbon nanotubes; sulfur resistance

1. Introduction

The water gas shift (WGS) reaction is a key operation in the industrial production of hydrogen from fossil fuel and biomass or biogas-derived syngas. The reaction, as expressed by Equation (1), is moderately exothermic and reversible. The WGS reaction rate is enhanced but the equilibrium CO conversion is lowered when increasing reaction temperature.

$$CO + H_2O \overset{cat}{\Leftrightarrow} H_2 + CO_2,\ \Delta H_r^o = -41.2\ \text{kJ/mol} \quad (1)$$

For the past decades, the concept of high-temperature H_2-permselective WGS membrane reactor (MR) has attracted tremendous interest because of its capability to overcome the limit of equilibrium conversion by instantaneously separating and removing the H_2 product from the catalyst bed during reaction. The H_2-permselective WGS MRs are thus widely viewed as a promising means to lower

costs of H_2 production with simultaneous CO_2 separation and capture because they enable significant process intensification and simplification for the reduction of energy consumption and capital cost [1].

In the past, substantial progress has been made in developing H_2-permselective membranes and WGS catalysts with hydrothermal stability and chemical resistance for processing the H_2S-containing syngas from fossil fuels and biogases. The group of transition metal-doped ferrite catalysts is well known for their excellent activity in catalyzing WGS reaction at high temperatures (350~550 °C). Various metal dopants in the ferrite catalyst have been used to enhance the kinetic rates, material stability, and tolerance to sulfur impurities in the feed gases [2]. Recently, we demonstrated a modified MFI-type zeolite membrane with long-term stability and a high H_2/H_2S separation factor for WGS MR operation at high temperature and pressure [3,4]. The combination of the ferrite-based catalysts with the H_2-permselective zeolite membrane was able to achieve near-complete CO conversion (χ_{CO} > 99.5%) under high reaction pressure (>15 bar) and temperature (~500 °C) with and without high H_2S content (>400 ppm) in the feed [5]. The high-temperature and high-pressure (HTP) conditions on the reaction side elevate the H_2 partial pressure on the reaction side ($p_{H2,r}$) that, with near-zero H_2 partial pressure on the permeate side ($p_{H2,p}$), maintains the driving force (i.e., $\Delta p_{H2} = p_{H2,r} - p_{H2,p}$) for maximum removal of H_2 through membrane permeation, which is necessary for approaching complete CO conversion [5]. In this case, the HTP reaction conditions may create extremely H_2-lean gas environments that are fundamentally different from that in the conventional packed bed WGS reactors or in most of the reported WGS MRs where H_2 removal is often far from completion. The HTP WGS MR operation conditions may become thermodynamically favorable for the CO carbonization and methanation reactions because of their volume reduction nature. Although WGS catalyst deactivation by surface coking has been known as a long-standing concern [6], carbon formation, especially the possible coproduction of valuable carbon nanomaterials on ferrite catalysts in HTP WGS MR reactions, has not been specifically investigated so far.

In the literature, Fe-based catalysts have been reported to produce graphitic carbon materials from CO and CH_4 gases [7–10]. The structure of the carbon products can vary broadly depending on the catalyst, feed gas composition, and reaction conditions, and often includes mixtures of carbon coatings, particulates, nanofibers, and nanotubes, etc. The carbon nanotubes (CNTs) are mostly produced by CVD of high-purity CO or hydrocarbons using metallic nanoparticle catalysts with or without oxide supports. The biogas and coal-derived syngas, however, often contains H_2S impurities, which can poison most WGS catalysts. The sulfur resistance of the doped ferrite catalysts for high-temperature WGS membrane reaction has been well documented in our previous reports [3,11]. However, the FeCr catalyst surface composition and chemistry during MWCNTs formation in the strongly reducing CO/CH_4 dry gas can dramatically differ from that in the HTP WGS MRs, where oxidizing steam exists. Sulfur can react with metallic iron to form FeS to lower the surface energy and inhibit aggregation and sintering of catalyst nanoparticles that consequently help in maintaining good chirality and dimensional uniformity of the resultant CNTs [12,13]. To take advantage of such beneficial effects, trace level sulfur compounds are formed in the catalyst prior to the CVD reaction of pure gas precursors. Metal sulfates, such as $FeSO_4$, $NiSO_4$, and $CoSO_4$, have been used as precursor to form sulfur-containing catalysts for CNT synthesis [13–16]. The sulfur contents in the catalyst surface were often not detectable by common characterization methods, such as energy dispersive X-ray spectroscopy (EDS) with scanning electron microscopy (SEM), transmission electron microscopy (TEM), and X-ray photoelectron spectroscopy (XPS), because of their trace amounts. Although trace FeS alloy in the metallic catalysts may facilitate CNT formation, excessive sulfur contents could adversely affect the catalytic activity. Therefore, the effects of H_2S impurity in the continuously fed gas flow and possible accumulative incorporation of sulfur into the originally sulfur-free catalyst on carbon formation during the CVD reactions of CO and CH_4 gases can be different and are currently not clear.

In this work, a Cr-doped ferrite (FeCr) nanocrystalline catalyst has been investigated for catalyzing MWCNT formation in a H_2-permselective MFI-type zeolite MR under HTP WGS membrane reaction conditions, where near-complete CO conversion is achieved by virtually total removal of H_2 product.

The FeCr catalysts are one of the most established HTP WGS catalyst with the Cr-dopant known to reduce the crystallite size and prevent nanoparticle sintering for long-term stabilization [17,18]. Based on the findings of the HTP WGS MR reactions, extended studies are carried out on the reactions of the FeCr catalyst with dry gases containing CO and CH_4, which are apparent sources in the WGS MR for direct carbonization on FeCr oxide surfaces. Experiments are also conducted for the CO/CH_4 dry gas containing a high content of H_2S that is practically important for the potential utilization of biogas and cheap coal-derived syngas.

2. Results and Discussion

2.1. MWCNT Formation in WGS MR

The WGS reaction was carried out in the FeCr catalyst-packed MR at 500 °C as a function of time and reaction side pressure, and the results are presented in Figure 1. The χ_{CO} of the MR increased continuously with reaction side pressure while the permeate side sweep flow remained at atmospheric pressure. Such a χ_{CO} dependency on the reaction pressure can be attributed to the prolonged residence time, accelerated reaction rate, and enhanced H_2 membrane permeation rate under increased reaction pressures at a fixed gas hourly space velocity (GHSV) [4,5]. At GHSV = 7500 h^{-1} and steam-to-CO ratio $R_{S/CO}$ = 3.5, the MR achieved CO conversion χ_{CO} > 99.5% when operating at reaction side exiting pressure $P_{r,ex}$ of >15 bar. As can be seen in Figure 1a,b, near-complete CO conversion was obtained with almost total hydrogen recovery R_{H_2} (~99%) at a cost of significantly lowered H_2 concentration in the permeate (y_{H_2}) due to the membrane's limited H_2/CO_2 selectivity $\alpha_{H2/CO2}$ ~ 25. During the MR operation, the $P_{r,ex}$ was maintained at each preset value while the pressure of feed entrance ($P_{r,in}$) was elevated to keep the GHSV constant when the resistance to gas flow in the catalyst bed increased continually by the accumulating carbon deposits. Figure 1a shows that $P_{r,ex}$ was able to stabilize to below 15 bar without large adjustments for $P_{r,in}$, indicating that carbon deposition was insignificant or very slow under relatively low reaction pressures, which is consistent with the findings on similar Cr-doped ferrite catalysts [5,11]. However, when the $P_{r,ex}$ reached ~20 bar, where χ_{CO} exceeded 99.5% at R_{H_2} of ~99%, the $P_{r,in}$ rapidly increased in order to keep GHSV unchanged. The MR operation was terminated at $P_{r,in}$ of ~30 bar around which the GHSV was no longer able to stabilize as the tube side catalyst bed became tightly clogged by the accumulated carbon deposits; meanwhile, shortly after reaching χ_{CO} > 99.5% at $P_{r,ex}$ of >15 bar, the χ_{CO} started to drop sharply with time because of severe catalyst deactivation by carbon coverage. The fast decline of χ_{CO} occurred similarly for feeds of higher GHSV (e.g., 15,000 and 30,000 h^{-1}) and/or lower $R_{S/CO}$ (e.g., 1.5) when the MR was operated at 500 °C and 20 bar (see Figure S1). The χ_{CO} of the WGS MR was able to reach >99.5% at GHSV = 15,000 h^{-1} and $R_{S/CO} = 3.5$ but not for GHSV = 30,000 h^{-1} with $R_{S/CO} = 3.5$ or for GHSV = 15,000 h^{-1} with $R_{S/CO} = 1.5$ because of shortened residence time at greater GHSV (=30,000 h^{-1}) or lowered equilibrium CO conversion for the smaller $R_{S/CO}$ $(= 1.5)$.

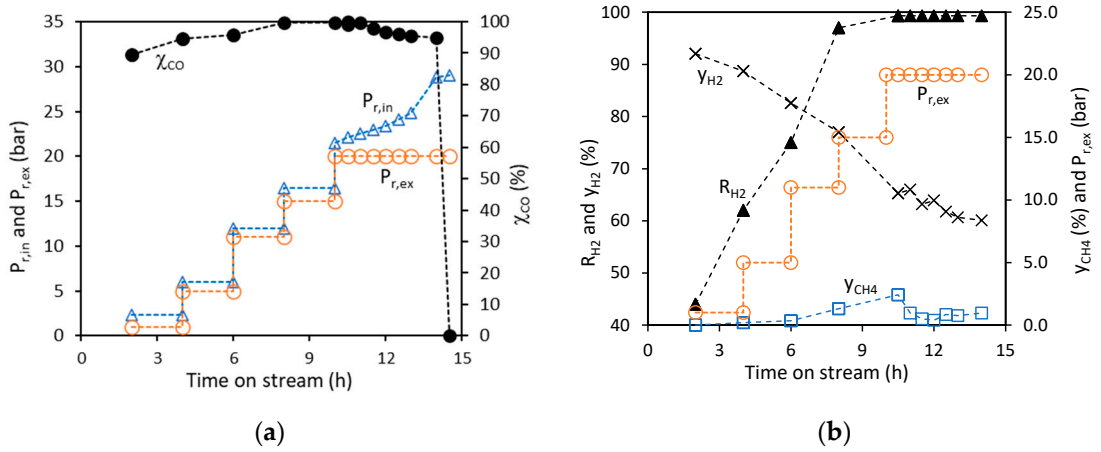

Figure 1. Results of WGS reaction at 500 °C in the zeolite MR as a function of time-on-stream with correspondingly increasing reaction pressure and constant atmospheric pressure on the permeate side: (**a**) χ_{CO} and corresponding $P_{r,in}$ and $P_{r,ex}$, and (**b**) R_{H2} and y_{H_2} in permeate and y_{CH4} in retentate.

In Figure 1b, the dry gas-based mole fraction of the byproduct CH_4 in the reaction side (y_{CH4}) was quite low (y_{CH4} < 2.5%) but increased monotonically with the rising reaction pressure up to ~20 bar. The CH_4 was virtually undetectable in the permeate stream because of its very small permeation rate. This pressure dependency of y_{CH4} in the MR may be explained by the fact that the methanation increases with pressure because of the volume reduction reactions and, on the other hand, methanation is mitigated by timely removal of the produced H_2, which is a precursor for CH_4. Immediately after χ_{CO} reached near-completion (>99.5%) at 20 bar, the y_{CH4} exhibited a trend of decreasing and then slightly increasing with operation time. Such a drop of methanation rate was also observed in other WGS MR reaction conditions in Figure S1, though the subsequent increase of y_{CH4} after the initial drop at 20 bar was not always appreciable likely because of the fast carbon deposition rate at ~20 bar that led to fluctuation of gas flowrate and consequently large deviations in determining the y_{CH4}. Nevertheless, the unique y_{CH4} dependency on operation time and reaction pressure indicate the involvement of CH_4 or chemisorbed intermediates (e.g., surface CH_x, $0 \le x < 4$ [19,20]) in carbon formation during HTP WGS reaction in the MR.

Structures of the carbon products. After terminating the WGS reaction upon the rapid $P_{r,in}$ increase, the MR was cooled down in a continued N_2 purging gas flow, and the membrane tube was carefully opened to observe the status of the packed bed along the tube. A highly compacted carbon/catalyst bed segment was found in the first half of the active membrane section, with the other half near the exit also filled with carbon materials but less tightly packed. The solid materials of the catalyst bed were quickly retrieved and sealed in glass vials, within 20 min, for various tests to identify the types of carbon and characterize the properties of both the catalyst and carbon products.

The SEM image in Figure 2a shows that the solid product was CNTs with lengths of a few microns and diameters in a broad range from ~10 to over 50 nm. The results of Raman shift characterization shown in Figure 2b indicate a D/G intensity ratio (I_D/I_G ~ 1.03) of the carbon materials that was typical to the MWCNTs synthesized by oxide catalyst via the CVD method. The TEM images in Figure 2c reveal that the carbon products were MWCNTs with wall thickness and graphene layer structure that are also similar to those formed on oxide catalysts, which are generally of low chirality and crystallinity and short length. The TEM image in the insert of Figure 2c suggested a tip-growth mechanism for the MWCNTs on the FeCr oxide catalyst. The MWCNTs, in this case, grew in the free end, i.e., tip growth mode, and the diameter was apparently defined by the catalyst particle size as shown by the SEM and TEM images in Figure S2. The composition of the MWCNTs measured by the EDS technique had a C/(FeCr) atomic ratio of ~119 and a mass ratio of ~70 assuming that the catalyst had a partially reduced state of Fe_3O_4. The element Cr was hardly seen in the EDS spectrum in Figure 2d, likely because of its overall extremely low content in the sample of largely carbon contents.

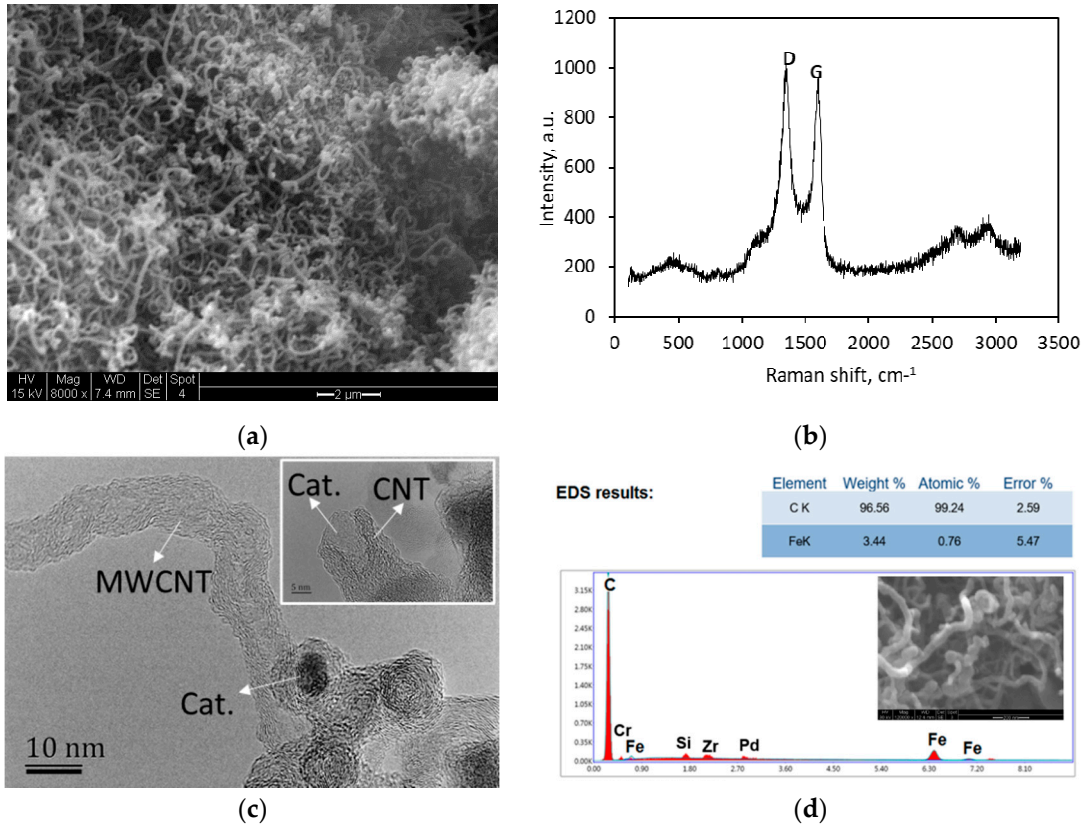

Figure 2. Characterizations for the carbon/catalyst materials formed in the HTP WGS MR: (**a**) SEM image, (**b**) Raman shift, (**c**) TEM image, and (**d**) SEM–EDS results.

States of the catalysts. The mechanisms of CNT tip-growth on oxide and metallic particles are different with the former depending on surface chemisorption followed by surface migration of carbonaceous intermediates, and for the latter, involving carbon dissolution as metal carbides and diffusion through metallic body to supply the CNT growth [21,22]. The oxidation states of the metal elements in FeCr catalysts were examined using the XPS technique for samples in different stages of processing. The XPS investigation was also used to provide evidence for the involvement of CO and CH_4 in catalytic carbon formation on the catalyst. Figure 3 displays the XPS spectra for catalyst samples including (1) the as-synthesized FeCr catalyst denoted as "Fresh FeCr", (2) the catalyst after activation in the reducing process gas denoted as "Reduced FeCr", (3) catalyst after WGS reaction in the MR denoted as "Reacted FeCr", and (4) a catalyst containing no Cr dopant named as "Reacted FeOx", which was similarly activated and treated by WGS reaction processes to provide a reference.

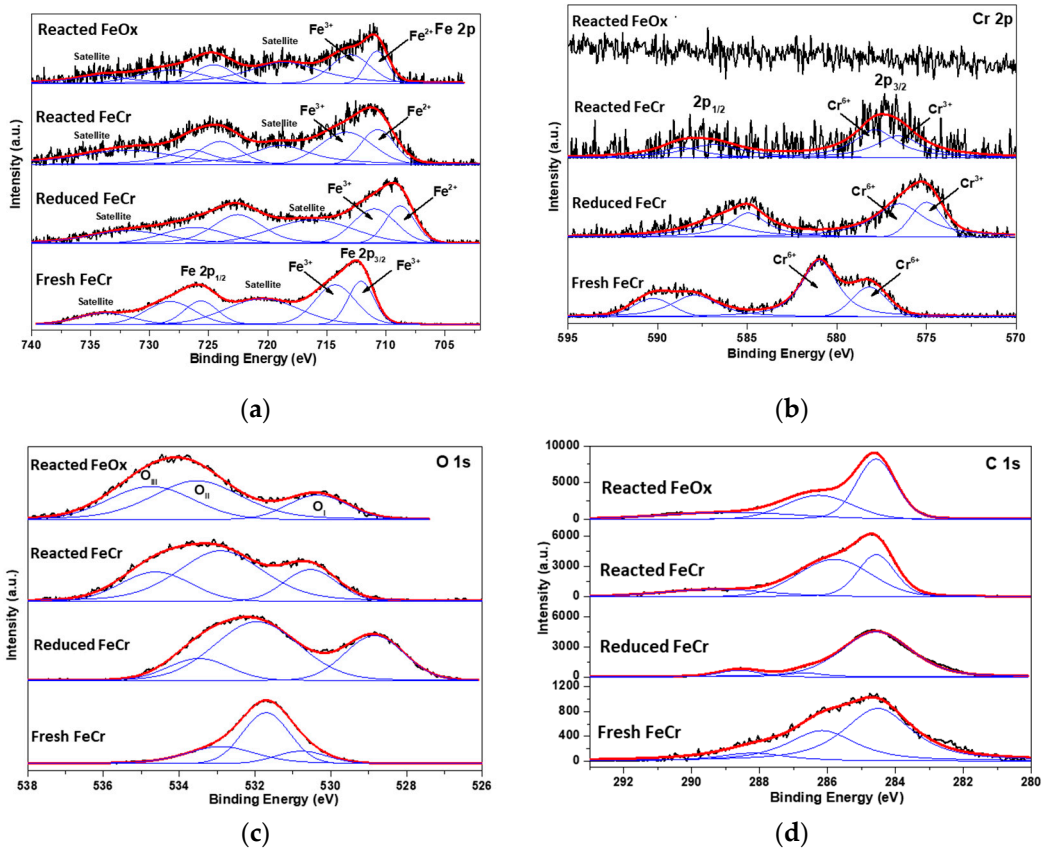

Figure 3. XPS spectra of the FeCr catalyst samples at various stages of processing: (**a**) the Fe 2p XPS spectra, (**b**) the Cr 2p core-level XPS spectra, (**c**) the O 1s spectra, and (**d**) the C 1s spectra.

In Figure 3a, the Fe 2p XPS spectrum of the fresh FeCr contains two distinct peaks at 712.5 eV for Fe $2p_{3/2}$ and at 725.9 eV for Fe $2p_{1/2}$ along with two satellites at 720.4 and 734.0 eV that indicate the presence of α-Fe_2O_3 phase in the sample. Although the reduced and reacted catalysts exhibited similar peaks like in the fresh sample, the binding energies of the Fe $2p_{3/2}$, Fe $2p_{1/2}$, and satellite bands were shifted to lower values. These shifts can be attributed to the formation of Fe_3O_4 phase in the reduced and reacted FeCr catalysts. Further, the Fe 2p spectra were deconvoluted using the Gaussian–Lorentzian line shape and the fitted results show that the peak of Fe $2p_{3/2}$ and Fe $2p_{1/2}$ core-level electrons split into two components in all the catalysts. In particular, the fitted peaks of Fe $2p_{3/2}$ indicate the presence of mixed $Fe^{3+/2+}$ valence states in the reduced and reacted catalysts but not in the fresh sample. This confirms pure Fe_2O_3 phase for the fresh catalyst and the existence of Fe_3O_4 phase in the reduced and reacted samples. The Fe $2p_{3/2}$ envelope does not show any appreciable peak at around 708 eV, indicating the absence of metallic Fe (Fe^0). Figure 3b presents the Cr 2p core-level XPS spectra of FeCr catalysts in contrast to the Cr-free sample of FeOx, which has no peaks in the Cr 2p region. In the spectra of the FeCr samples, the spin-orbit splitting of the XPS spectra shows a double $2p_{1/2}$ and $2p_{3/2}$ excitations. The fitted Cr $2p_{3/2}$ spectrum of fresh catalyst exhibits peaks at about 580.9 and 578.1 eV, which are assigned to the Cr^{6+} species. On the other hand, the deconvoluted Cr $2p_{3/2}$ spectra of reduced and reacted FeCr catalysts indicate the presence of both Cr^{6+} and Cr^{3+} states. Moreover, the binding energy of the reduced and reacted samples was blue-shifted from that of the fresh sample. This could be due to the existence of more Cr^{6+} species in the fresh catalyst that have higher electronegativity than the Cr^{3+} species.

The deconvoluted O 1s spectra of all samples exhibited three peaks in Figure 3c, which are assigned as O_I, O_{II}, and O_{III}. The O_I peak is ascribed to the lattice oxygen, while the O_{II} and O_{III} bands respectively correspond to the surface-adsorbed oxygen species and weakly bonded oxygen species, like molecular water or carbonate species, on the catalysts. The C 1s spectrum is usually

expected from the background carbon tape used during the XPS analysis. However, the intensities of the C 1s peaks from the reduced and reacted catalysts in Figure 3d were far greater than that of the fresh sample, which only exhibits weak background carbon peaks. The dramatic change of C 1s peak intensity is indicative of carbon formation during the activation (reduction) and WGS reaction processes. Moreover, the reacted catalysts exhibited the highest C 1s peak intensity that suggests more carbon formed on the surface as compared to the reduced sample. The fitted C 1s spectra of the samples show the peaks at 284.6, 285.6–286.8, and 288.3–289.6 eV, which can be attributed to C–C and/or C–H bonds, carbon linked to one O atom by a single bond (C–OH, C–O–C, C–O–R) or a double bond (–C=O), and carbon attached to two oxygen atoms (–COOH), respectively.

The above XPS analyses of the FeCr catalysts at different processing states indicate that the Fe^{3+} and Cr^{6+} were partially reduced to Fe^{2+} and Cr^{3+} to form Cr-doped ferrite (Fe_3O_4) after being activated in the reducing gas flow. The XPS spectra of the solid products from the WGS membrane reaction revealed C–C and C–H bonds formed in the surface carbonaceous species and O–C and O–CH_x in the catalyst surface. These carbonaceous species are common intermediates of nonoxidative dehydrogenation of CH_4 on oxide-promoted metal catalysts [20]. It is evident that during the WGS MR reaction, carbon formation from both CO and CH_4 or methanation intermediates occurred in the catalyst surface under H_2-lean HTP conditions. However, it is not clear whether the two apparent carbon sources, namely CO and CH_4, had synergistic or interdependent effects in MWCNT growth on the catalyst surface. The XPS and TEM results showed no direct evidence of metallic elements, suggesting that the limited reducing power of gases containing high-concentration steam and CO_2, which are weakly oxidative, is unable to further reduce the Fe^{2+} to Fe^0.

2.2. Reaction of Dry Source Gases on FeCr Catalysts

The chemical analyses of the gas products and XPS examinations of the solid products from the HTP WGS membrane reaction have suggested the involvements of CO disproportionation, Reaction (2), and CH_4 dehydrogenation, Reaction (3), in MWCNT growth on the FeCr catalyst.

$$2CO \overset{cat.}{\leftrightarrow} CO_2 + C, \quad \Delta H_r^o = -173 \text{ kJ/mol} \tag{2}$$

$$CH_4 \overset{cat.}{\leftrightarrow} C + 2H_2, \quad \Delta H_r^o = +74.9 \text{ kJ/mol} \tag{3}$$

Reaction (2) is favored at high pressure by its volume reduction effect. Reaction (3) is, however, a volume increase process but can be facilitated by instantly removing the product H_2 from the catalyst through selective membrane permeation. On the other hand, the removal of H_2 from the catalyst zone could inhibit the methanation processes, which could include the following reactions [4,23]:

$$CO + 3H_2 \overset{cat.}{\leftrightarrow} CH_4 + H_2O, \quad H_r^o = -206 \text{ kJ/mol} \tag{4}$$

$$CO_2 + 4H_2 \overset{cat.}{\leftrightarrow} CH_4 + 2H_2O, \quad H_r^o = -164 \text{ kJ/mol} \tag{5}$$

The rapid decline of CH_4 content upon carbon formation in the WGS MR at 20 bar, as shown in Figure 1b and Figure S1, may be attributed to sudden catalyst deactivation by the fast carbon deposits. Although the catalytic methane decomposition could involve complicated serial reaction steps [24], the whole process of carbonization via the routes of methanation and CH_4 decomposition must have overall stoichiometric mass balance and overall energy effect the same as the CO disproportionation Reaction (2) when WGS Reaction (1) is the H_2 source for Reactions (4) and (5).

Experiments on the feeds of CO and CH_4 single gas, a mixture containing 80 v.% CO and 20 v.% CH_4, and the CO/CH_4 gas mixture containing 500 ppmv H_2S were conducted to investigate the FeCr catalytic activities in these conditions. The CO/CH_4 mixture composition of 80 v.% CO was selected because the pre-membrane catalyst bed together with the long stainless steel tubing (with oxidized surface) was able to achieve a χ_{CO} of 78%–86% when operating at 500 °C with $P_{r,ex}$ of 15–20 bar, GHSV

of 7500 h^{-1}, and $R_{S/CO}$ of 3.5. This conversion would lead to a CO partial pressure of ~0.8 bar at the beginning of the membrane section. The 20 v.% of CH_4 was selected largely for balancing the binary mixture at ambient total pressure within the range of CH_4 partial pressures observed in the MR retentates. A total of 0.5 g FeCr catalyst was loaded uniformly along the tube length and activated in the same process gas flow as that used in catalyst activation for WGS MR reaction.

2.2.1. Pure CO Feed

The reaction of pure CO feed was performed at 500 °C when the reaction (feed) pressure was increased from 1 bar to ~22 bar and the exiting gas flowrate was maintained at ~5 cm^3 STP/min. The exiting gas composition was analyzed for estimating the CO conversion assuming that CO disproportionation was the only reaction. The GC measurement of the exiting gas composition was taken twice at each pressure, and the two measurements were about 1 h apart to determine the stability and consistency of the operation. A rapid decrease in CO conversion was observed when the reaction pressure exceeded 4.7 bar below which the CO conversion rate was stable, as shown in Figure S3a. Furthermore, the carbon products obtained below 4.7 bar, e.g., those obtained at ~1.0 bar, were primarily graphitic carbon coatings and particles, as shown in Figure S3b–e without CNTs. An experiment on the pure CO reaction was then conducted at 500 °C under reaction pressure of 5.1 bar with a feed flowrate of ~10 cm^3 STP/min. The results are presented in Figure 4. The CO conversion χ_{CO} was high but constantly declining with time (Figure 4a) apparently due to catalyst deactivation by increasing surface carbon coverage. The SEM and TEM results in Figure 4b show long MWCNTs grown on the FeCr catalyst particles with uniform diameters of 25–50 nm and wall thickness of 5–6 nm (insert in Figure 4b). The Raman shift spectrum in Figure 4c confirms that MWCNTs are of well-defined graphitic phase.

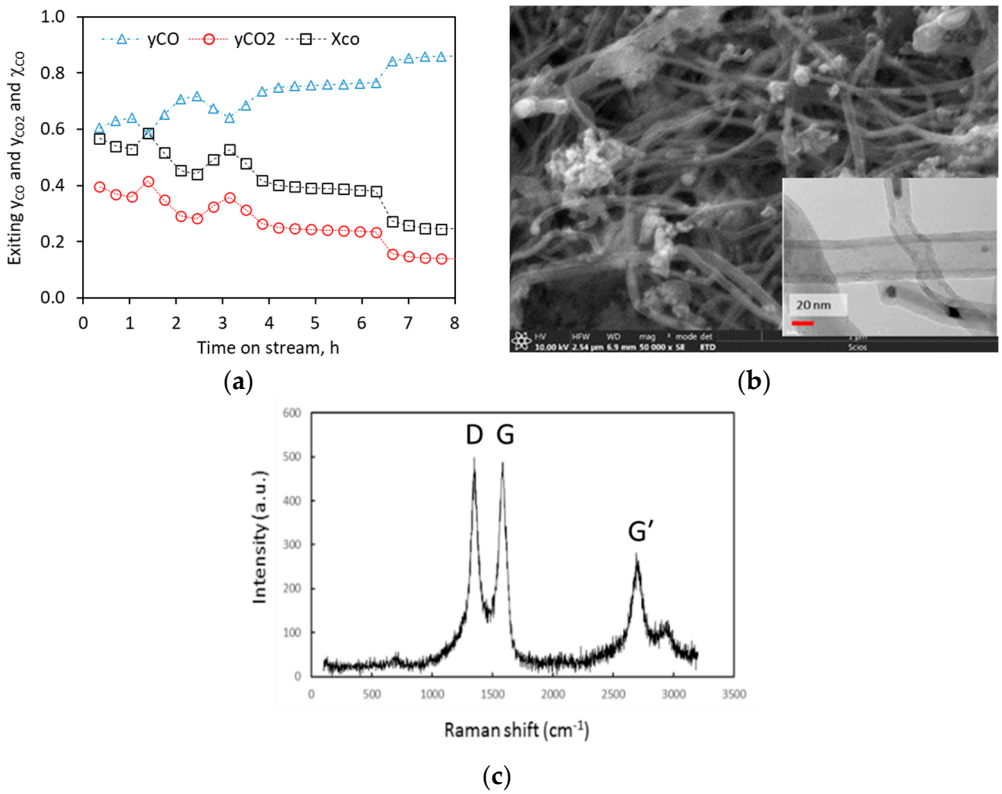

Figure 4. Results of MWCNT growth by CO reaction on the FeCr catalyst at 500 °C and 5.1 bar: (**a**) CO conversion and gas product composition as a function of reaction time, (**b**) SEM and TEM (insert) images of the MWCNTs, and (**c**) Raman shift spectrum of the produced MWCNTs.

2.2.2. Pure CH_4 Fee

For the CH_4 single gas feed, the reaction was first performed at 500 °C and 1 bar of total pressure. The feed CH_4 was carried in inert N_2 and the CH_4 partial pressure was changed by varying the CH_4 mole fraction in the CH_4/N_2 feed, and the feed gas flowrate was maintained at ~5 cm^3 STP/min. The compositions of CH_4 and H_2 in the gas product was monitored to estimate the CH_4 conversion. The GC measurement was performed twice for each CH_4 feed partial pressure over a period of 1 h after a stabilization period of at least 1 h. Figure 5a presents the CH_4 conversion as a function of CH_4 partial pressure in the feed. The CH_4 conversion was low and decreasing with increasing CH_4 feed concentration until the CH_4 partial pressure reached ~0.5 bar, above which the conversion remained virtually unchanged. The decrease of CH_4 conversion with feed pressure may be attributed to the reaction's volume increase effect and gradual catalyst deactivation by carbon coating. The gas flowrate was stable without adjusting the feed entering pressure even after a week of operation because of the very small amount of carbon deposition, which did not cause significant clogging of the catalyst bed. The SEM image of the solid products in Figure 5b shows no appreciable MWCNTs, and the EDS result in Figure 5c confirms a large amount of carbon materials on the FeCr catalyst. The peaks of Raman shift at small wavenumbers in Figure 5d suggest the existence of very small graphitic structures, but the peaks around 1500 cm^{-1} for the MWCNTs are hardly seen because of the lack of MWCNT products. An additional experiment was also conducted for pure CH_4 gas reaction with CH_4 pressure up to 5 bar under which the CH_4 conversion was also <0.5% with no MWCNTs. MWCNT formation by CVD decomposition of CH_4 on Fe catalysts has been reported at a higher temperature (e.g., 800 °C [25]) but clearly not at a low temperature (500 °C) for the FeCr catalyst. These results strongly suggest that CH_4 decomposition is very limited at such a low temperature and, thus, CH_4 was unlikely a main source for the fast MWCNT growth in the WGS MR.

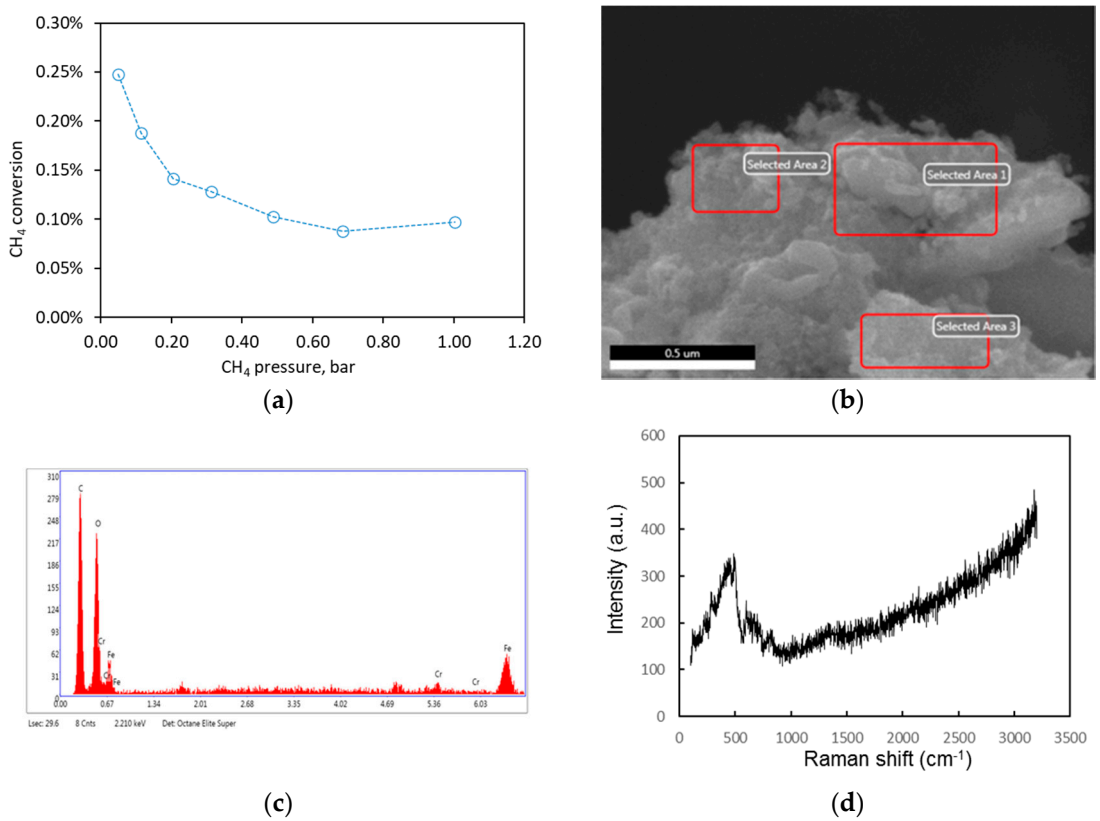

Figure 5. Results of pure CH_4 reaction on the FrCr catalyst: (**a**) CH_4 conversion as a function of feed CH_4 partial pressure, (**b**) SEM of the solid products, (**c**) the EDS elemental survey, and (**d**) the Raman shift spectrum for the carbon products.

2.3. CO/CH_4 Mixture Reaction and Effects of H_2S

2.3.1. CO/CH_4 Mixture Feed

For the feed of 80 v.%CO + 20 v.%CH_4 gas mixture, the experiments were performed at a feed flowrate of ~15 cm^3 STP/min when the reactor inlet and exit pressures were maintained at ~1.2 bar and atmospheric pressure (~1.013 bar), respectively. The reaction temperature was 500 °C, which was markedly lower than those required for CNT production by CVD on metallic catalysts from either of the single gases or the mixtures by [7,26–28]. The carbon deposition was found to be very fast and only one sample of the gas product could be analyzed after ~25 min of reaction when the drop in gas flowrate by carbon blocking was less than 30%. The reaction experiment was repeated three times, and the results were reasonably consistent in terms of the fast carbon formation, MWCNT morphology, and feed gas conversion. The molar compositions of CO and CH_4 in the gas product were 43.9% and 23.0%, respectively, that is reasonably consistent with the ~29.0% CO_2 and 4.1% H_2 according to the stoichiometric relations of possible reactions (2) and (3). The CO conversion was ~29.0% and CH_4 conversion was ~9.1% by calculations based on the CO and CH_4 composition changes. The gas flowrate started to decline sharply with time after just 30–40 min of reaction because of the fast growth of MWCNTs that blocked the catalyst-packed tube. The reaction was terminated at 1.5 h when the catalyst bed was severely blocked, and the gas flowrate dropped to below 3 cm^3 STP/min even when the entering feed pressure was increased to >3.5 bar. The ability of CO/CH_4 mixture to form CNTs with faster kinetic rates and higher conversions than the single gas feeds was previously observed in the literature and attributed to reactions (2) and (3) but at much higher reaction temperatures (>700 °C) [28]. The reaction Gibbs free energy (ΔG_r) of the exothermic CO disproportionation increases and that of the CH_4 decomposition decreases with increasing temperature with $\Delta G_r = -28$ kJ/mol for the former and $\Delta G_r = +12.4$ kJ/mol for the latter at 500 °C [29]. Thus, lowering reaction temperature increases the equilibrium conversion of CO and decreases that of CH_4, which may be the reason for the CO conversion being much higher than the CH_4 conversion in the reaction of CO/CH_4 mixture at low temperature (500 °C) and low feed flowrates. Carbon deposits from nonoxidative CH_4 dehydrogenation and/or CO disproportionation on oxide-supported metal catalysts can occur at relatively low temperatures to act as intermediates for both CO formation through carbon oxidation by CO_2 and re-hydrogenation of surface carbon in dry gas reforming of CO and CH_4 [19,20,29]. Because of the reactions' reversibility and common intermediates and products of these nonoxidative reactions, the reaction rates and carbon product morphological properties are expected to depend on mutual influences between CO and CH_4. Cofeeding CH_4 can also influence the reaction thermodynamics and kinetics through its H_2 product which, on the one hand, helps oxide reduction to create metallic components and, on the other hand, reduces the conversion rates and carbon yield by rehydrogenation of active carbon deposits [30]. The small amount of H_2O generated by CH_4 and H_2 from reduction of metal oxides could also reduce the amorphous carbon coverage on the Fe catalysts to preserve surface activity for growing longer MWCNTs [31].

Figure 6 shows the characterizations of the carbon products from the CO/CH_4 mixture reaction. The SEM and TEM images in Figure 6a,b reveal that the cleaned carbon products were MWCNTs without appreciable textures of graphitic particles or thick coatings. The MWCNT cleaning was done by sedimentation in ethanol solution for removal of the heavier glass fibers and large particles and subsequent dissolution of the exposed catalyst particles in 2 M HCl solution. The MWCNTs were found to have lengths in a range of 3–10 μm and diameters in a range of 15–35 nm. The high-resolution TEM images and interlayer spacing measurement in Figure 6b or Figure S4a,b show CNT walls consisting of highly ordered 11–13 graphene layers at an interlayer spacing of ~0.35 nm, which form a uniform wall thickness of 4–5 nm. The small I_D/I_G ratio of ~0.71 in the Raman shift spectrum of Figure 6c also indicates a high crystallinity of the MWCNs, i.e., larger crystallite size and high-degree order of the constituting graphene layers in the nanotube wall [32]. The EDS spectrum in Figure 6d focused on the MWCNT tips and the inserted values from large area survey of the clean sample both showed negligible

oxygen contents, suggesting the possible metallic form of iron nanoparticles enclosed in the MWCNTs due to further reduction of Fe^{2+} to Fe^0 in the strongly reducing CO/CH_4 dry gas. The characteristic peaks of Cr were inappreciable, which may be a result of its extremely low content in the sample or removal by solid phase separation during the reduction process since Cr^0 was not formed to alloy with Fe^0. The full understanding of the chemical state and microstructure evolution of the FeCr catalyst during the reaction process is currently unclear and requires further investigation through in operando reaction measurements and in situ TEM and XPS examinations. The TGA/DTA measurement of the raw sample of MWCNTs, as shown in Figure S4c, indicated ~46% MWCNTs due largely to the inclusion of glass fibers and catalyst particles of very large sizes. The relatively low temperature of carbon combustion, which is common in the literature for CNTs made by the CVD method, may be attributed to the exposed metal oxides in the raw sample, which could catalyze the CNT oxidation at low temperatures [33].

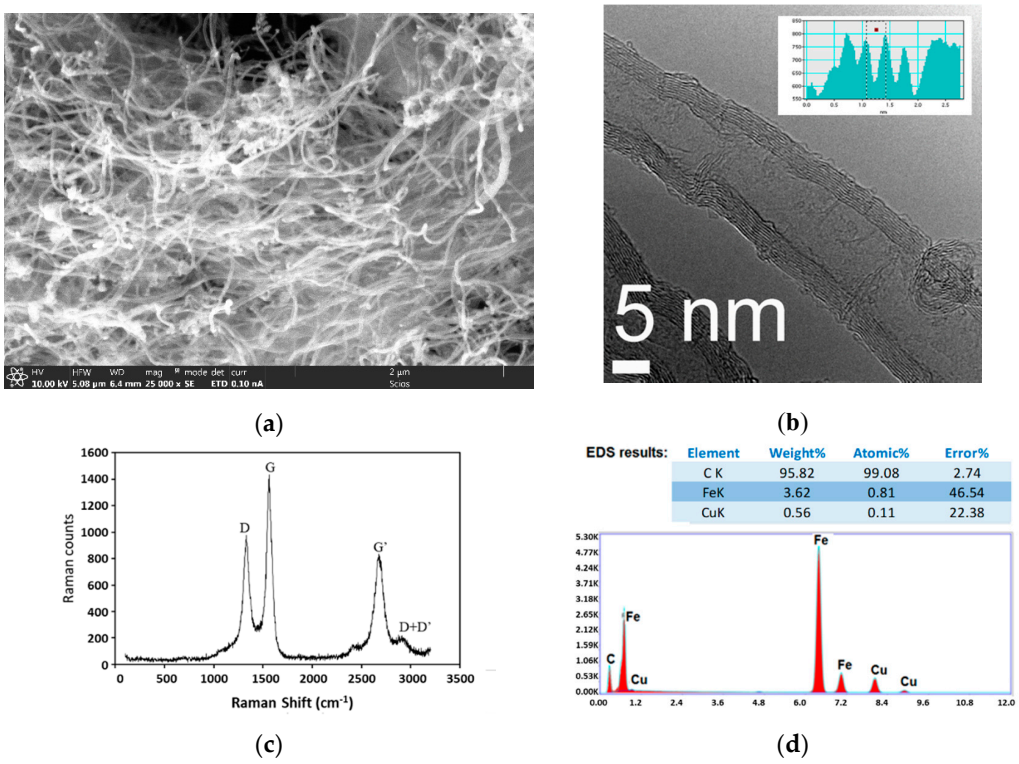

Figure 6. Characterizations of MWCNTs formed from the CO/CH_4 mixture: (**a**) SEM image, (**b**) TEM image showing typical MWCNT diameter and wall thickness, (**c**) Raman shift spectrum of the MWCNTs, and (**d**) EDS measurement focusing on MWCNT tips (insert survey over a large sample area).

In comparison with the observations on CO and CH_4 single gas reactions, it can be inferred from the results of CO/CH_4 mixture reaction that synergistic effects between the CH_4 and CO promoted MWCNT formation and enhanced the reaction rates. Literature studies have shown that the rates of CNT formation can be represented by semiempirical models that correlate the CO and CH_4 reactions through kinetic and thermodynamic interactions of the common reactants/products [26]. Similar effects of CO/CH_4 mixture feeds on lowering temperature for carbon deposition and enhancing feed conversion as compared to the single gas feeds were also reported for the Mg-incorporated alumina-supported Ni nanoparticle catalyst, but the resultant MWCNs appeared to be of low crystallinity and dimensional uniformity [34]. However, fundamental understandings on the relationships between the produced carbon structure and the reaction conditions (including the CO/CH_4 feed composition as well as reaction temperature and pressure) and the catalyst type is currently challenging. In this study, the FeCr catalyst in the carbon product from CO/CH_4 mixture reaction was also examined by XPS to help understand the MWCNT formation process, which is discussed in the following section.

2.3.2. Effects of H_2S in Feed

To investigate the influence of sulfur contents in the feed on the performance of the FeCr catalyst, reactions were performed for the 80v%CO + 20v%CH_4 mixtures containing 500 and 800 ppmv of H_2S, respectively. The rates of carbonization reactions decreased in the presence of H_2S. The catalyst-packed tube was blocked by the carbon products in 3–4 h when the gas flowrate started to drop drastically after ~2 h of reaction. Based on the gas product composition measured after the initial 60 min operation, the conversions of CO and CH_4 were ~6% and <1%, respectively, for the feed with 500 ppmv H_2S, which decreased from those in reaction of the mixture without H_2S. Figure 7 shows the SEM and TEM images and the Raman shift spectrum of the carbon products generated from the feed with 500 ppmv H_2S, which was cleaned by two days of treatment in 2 M HCl solution under stirring. The carbon products were predominantly long and uniform MWCNTs of good crystallinity indicated by the small I_D/I_G ratio (~0.80), which are very similar to those formed from the sulfur-free CO/CH_4 mixture. The TEM images in Figure 7b indicate that the MWCNTs had an average diameter of ~25 nm with 4–5 nm thick walls of highly aligned graphene layers. The EDS results of the MWCNTs after removing glass fibers and large particles but before cleaning by acid washing (Figure S5) confirmed the existence of significant sulfur content in the carbon/catalyst sample. However, the reaction of CO/CH_4 mixture with 800 ppmv H_2S resulted in carbon products mainly in the forms of thick graphitic coatings and particles with few MWCNTs (Figure S6). These morphological and structural properties of the MWCNTs are very similar for those produced by the feeds with and without the 500 ppmv H_2S. This indicates that the FeCr catalyst has good sulfur resistance in catalyzing the MWCNT formation, but the reaction rates can be decreased by the presence of H_2S. The apparently decreased reaction rates of the H_2S-containing feeds may be a result of the loss of catalytically active sites due to the chemisorption of sulfide. It was found that CO chemisorption uptake on the FeCr catalyst declined significantly after being treated by H_2S at 500 °C (see Figure S7). The FeCr catalyst was also found to lose specific selectivity towards the MWCNT product for feeds with very high H_2S contents (e.g., 800 ppmv).

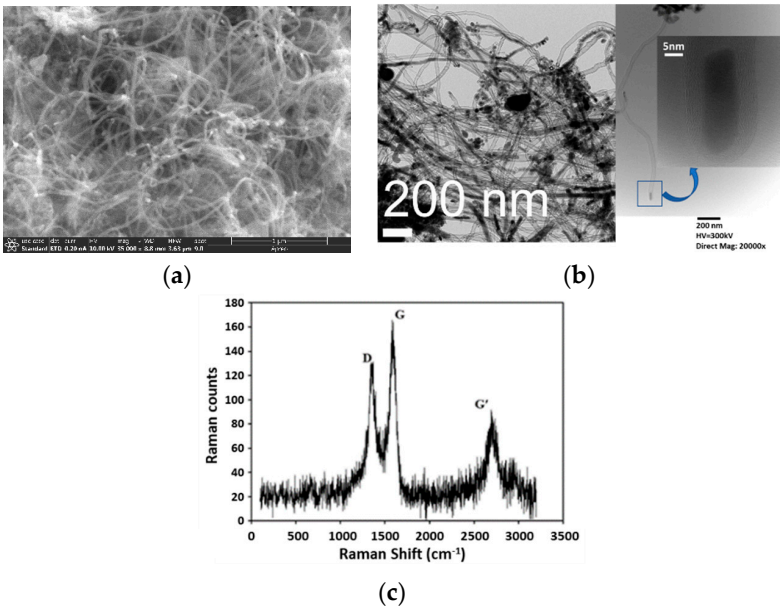

Figure 7. The MWCNTs produced by the FeCr catalyst at 500 °C and 1 bar from the 80%CO + 20%CH_4 mixture feed with 500 ppmv H_2S: (**a**) SEM image, (**b**) TEM images, and (**c**) Raman shift spectrum.

Compared to the MWCNTs formed on the FeCr catalysts in the HTP WGS MR, the MWCNTs obtained from the CO/CH_4 dry gas mixtures with or without H_2S impurity (500 ppmv) were apparently of larger length, better chirality and uniformity, and greater crystallinity. The XPS Fe 2p spectra in Figure 8a clearly show the presence of metallic iron (Fe^0) in the catalyst samples after reaction with the

CO/CH_4 gas mixture with and without H_2S contents. The formation of metallic Fe component was not seen in the catalysts after HTP WGS membrane reaction (Figure 3). The further reduction of Fe^{2+} to Fe^0 evidently occurred in the CO/CH_4 dry mixtures because the dry environment is more reductive than the steam-containing gas in the HTP WGS reaction [35]. The metallic iron nanoparticle or surface, which can form iron carbides and allow diffusion of carbon atoms to sustain the CNT growth, may be the main reason for the formation of highly crystalline MWCNTs from the CO/CH_4 dry mixture. However, the characteristic XPS peaks of iron carbides ($Fe_{1-x}C_x$) around 285–295 and 710–722 eV overlap with the strong peaks of carbonaceous compounds in C 1s and Fe $2p_{3/2}$ spectra, respectively [36]. Hence, the iron carbides would not be distinguishable due to the expected minimal mass amount, even if they existed. The XPS results in Figure 8b indicate that further reduction of Cr^{3+} to Cr^0 did not happen in the CO/CH_4 dry gases. These findings suggest that the FeCr catalyst formed metallic Fe nanoparticles supported on $Fe^{3+/2+}$ and $Cr^{6+/3+}$ oxides in which the oxide surface inhibited the migration and aggregation of metallic particles that may have, in turn, improved the MWCNT uniformity [37].

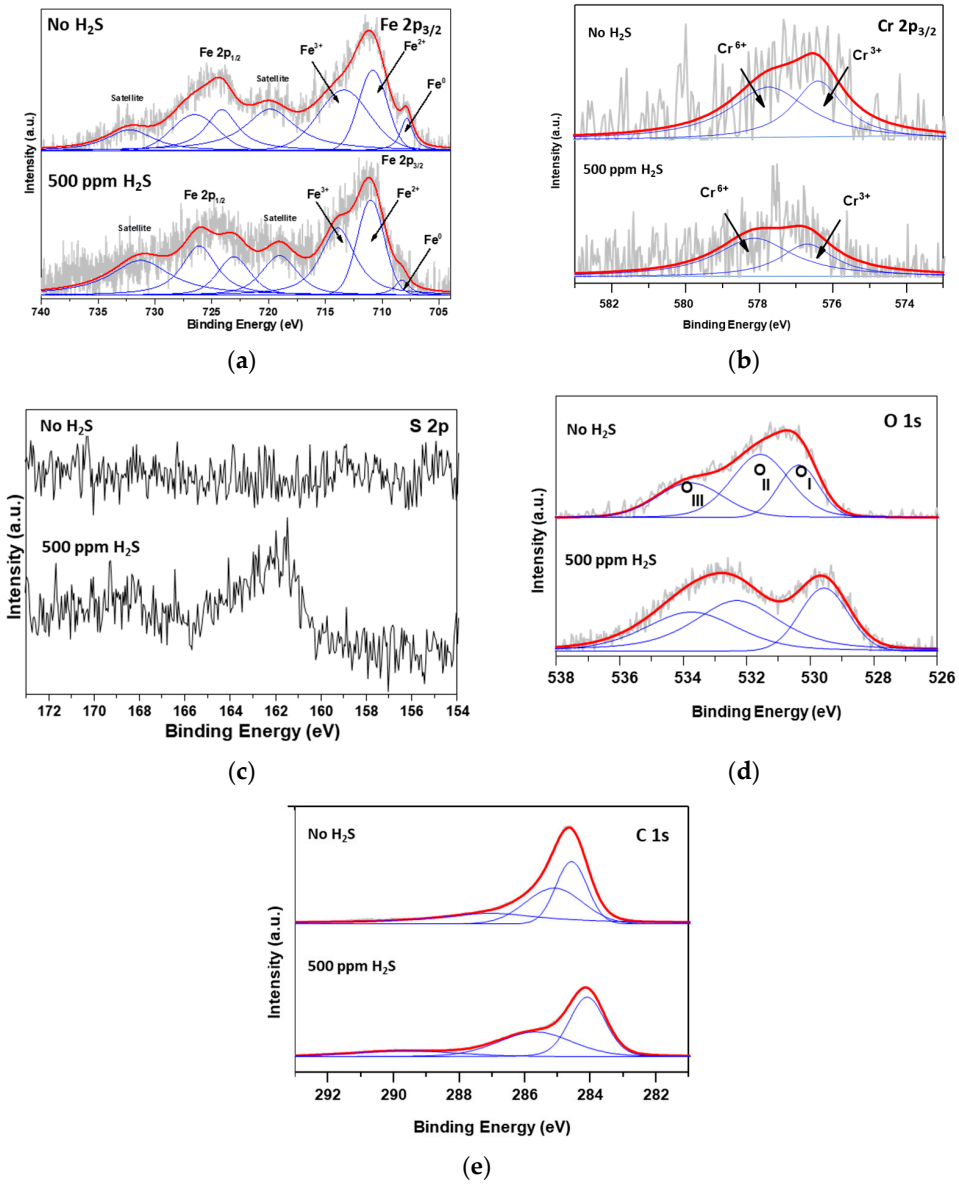

Figure 8. XPS spectra of the FeCr catalysts after reacting with the CO/CH_4 mixture with and without 500 ppmv H_2S: (**a**) Fe $2p_{3/2}$ spectra, (**b**) Cr $2p_{3/2}$ spectra, (**c**) O 1s spectra, (**d**) C 1s spectra, and (**e**) S 2p spectra.

The spectra of S 2p in Figure 8c clearly show the peak of S^{2-} at 158.5–165.7 eV for the sample reacted with the 500 ppmv H_2S but not in the sample reacted with the sulfur-free gas. The sulfide ion (S^{2-}) is likely chemisorbed on the surfaces of the catalyst and/or MWCNT. The XPS spectra in Figure 8d,e indicate that the presence of trace sulfur in the catalyst surface did not cause notable changes to the types of chemical bonds formed by CO and CH_4 reactions on the catalyst surfaces. These observations demonstrated that the existence of H_2S impurity in the CO/CH_4 feed gas with contents as high as 500 ppmv can introduce sulfur (S^{2-}) into the catalyst or carbon surfaces but not seriously influence the formation and morphological properties of the MWCNT products. However, the rates of CVD reactions are obviously slowed by the presence of the H_2S in gas phase, which may be chemisorbed on the catalyst surface to reduce the population of active catalytic sites. Extremely high contents of H_2S (e.g., 800 ppmv) can diminish the FeCr selectivity towards MWCNT products.

3. Materials and Methods

3.1. Catalyst Preparation

The nanocrystalline Cr-doped ferrite (FeCr) catalyst with an atomic ratio of Fe:Cr = 10:1 was prepared by the coprecipitation method following the procedure described in our earlier work [11]. This particular Fe/Cr ratio was chosen because it was previously found to have the smallest crystallite size and exhibit high catalytic activity among several doped ferrite catalysts in high-temperature WGS reaction [17,18]. In brief, during catalyst synthesis, the calculated amounts of iron nitrate and chromium nitrate with Fe:Cr atomic ratio of 10:1 were dissolved separately in DI water to form two solutions, which were subsequently mixed. A dilute aqueous ammonia solution was added to this mixed solution under stirring until precipitation was complete at a pH value of ~9. The resultant solid precipitates were recovered by filtration after overnight aging. The recovered solid was dried at 80 °C for 12 h followed by a 3-hour calcination at 500 °C in nitrogen atmosphere using heating and cooling rates of 5 °C/min. The SEM image in Figure 9a shows that the as-synthesized FeCr oxide particles were agglomerated nanoparticles. The TEM image in Figure 9b shows that the vast majority of primary particles had sizes of 15–25 nm. The Fe:Cr atomic ratio of the FeCr catalyst was confirmed to be around 11 ± 1.3 by SEM–EDS measurement (Figure S7), which was in reasonable agreement with that of the precursor solution (Fe:Cr ~ 10:1).

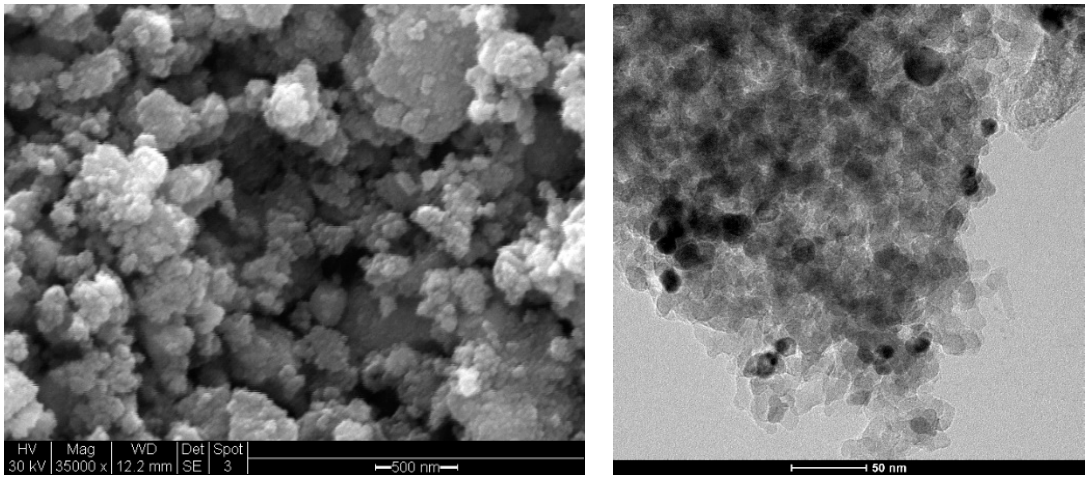

(**a**) (**b**)

Figure 9. The as-synthesized FeCr catalyst: (**a**) SEM image and (**b**) TEM image.

3.2. Membrane Fabrication

The MFI-type zeolite membrane was synthesized on the outer surface of a commercially available porous α-alumina tube (MPT Inc., Pittsburgh, PA, USA). The tube had an outer diameter (OD) of

0.57 cm, an inner diameter (ID) of 0.37 cm, and a total length of 10 cm with a 2.5 cm long glaze-sealed section in each end to give a 5 cm middle section coated with an active membrane area A_m = 8.95 cm^2. The tubular zeolite membrane synthesis, modification, and characterization processes have been explained in our previous publications [5,38,39], and a brief description is provided together with the SEM images of the membrane in Figure S8 of the Supplementary Materials. The MFI zeolite membrane layer had a thickness of ~7 μm. The zeolitic pore openings were reduced from the original diameter of 0.56 to <0.36 nm by deposition of monosilica in the zeolite channels via the catalytic cracking deposition (CCD) method. The thus-narrowed zeolitic channels enable size exclusion effects to enhance the H_2 permeation selectivity over CO and CO_2 [39,40]. The modified zeolite membrane used in this work had a H_2 permeance ($P_{m,H2}$) of ~1.02×10^{-7} mol/s·m^2·Pa with H_2 permeation selectivity over CO ($\alpha_{H2/CO}$), CO_2 ($\alpha_{H2/CO2}$) and H_2O ($\alpha_{H2/H2O}$) of 33 ± 5 and 25 ± 3 and 5 ± 2 respectively, at 500 °C. The gas permeance is defined as

$$P_{m,i} = \frac{Q_i}{A_m \cdot \Delta P_i} \quad (6)$$

where Q_i (mol/s; $i = H_2$, CO, CO_2, H_2O) is the flowrate of gas i through the membrane and $\Delta P_i = P_{i,f} - P_{i,p}$, where $P_{i,f}$ and $P_{i,p}$ are the gas partial pressures in the feed and permeate side, respectively. The H_2 separation selectivity over gas i ($\alpha_{H2/i}$) measured by mixture gas permeation is given by

$$\alpha_{H2/i} = \frac{(y_{H2}/y_i)_p}{(y_{H2}/y_i)_f} \quad (7)$$

where y_{H2} and y_i are gas mole fractions and subscripts p and f denote permeate and feed, respectively.

3.3. Reactors and Operations

The WGS reaction in the zeolite MR was carried out at 500 °C to study the FeCr catalyst activities for simultaneously producing H_2 and MWCNTs. The MR—which is a stainless steel module with the tube membrane mounted in the tube-in-shell structure—and the gas streams were in countercurrent crossflow configuration, as shown in Figure 10. The membrane tube was sealed in the MR by graphite gaskets. A total amount of ~0.7 g FeCr catalyst particles (packing density ~2.9 g/cm^3) were mixed with quartz wool and packed inside the tube as schematically illustrated by the insert in Figure 10. The catalyst bed started approximately 0.5 cm after the tube entrance, i.e., ~2.0 cm before the active membrane section and was evenly distributed along the entire membrane section. The MR was installed in a reaction testing system schematically shown in Figure 10. The pre-membrane catalyst bed, which converts a significant amount of CO before entering the membrane section, is necessary for membranes of moderate $\alpha_{H2/CO}$ to lower the reaction side CO partial pressure at the beginning of the membrane for preventing excessive permeation of unreacted CO. The WGS and dry gas reactions are exothermic overall, which may cause temperature increases to induce instability and affect reactor performance [41]. However, the small ceramic tube reactor, because of the large stainless steel housing and minimal amount of catalyst used, was able to stabilize the operation, with the exiting gas temperature increases being limited to <10 °C.

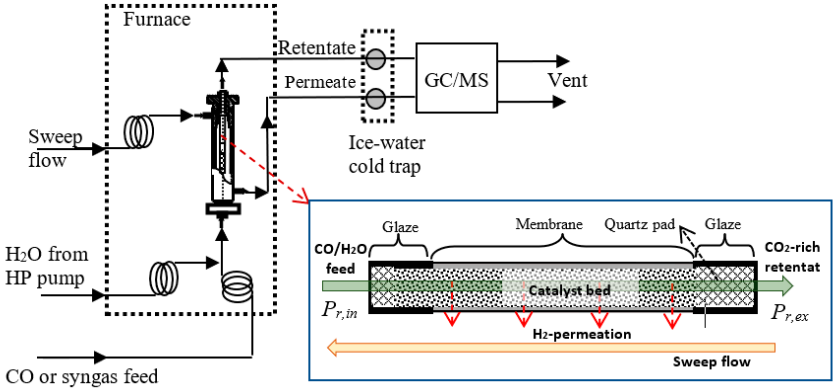

Figure 10. Schematic diagram of the WGS MR reaction system with an insert depicting the catalyst packing structure and countercurrent gas flow configuration.

The catalyst was activated after being packed in the MR by partial reduction at 400 °C for 4 h in a process gas flow containing 33.3% CO, 25.0% CO_2, 25.0% H_2, and 16.7% H_2O [4]. The WGS membrane reaction was performed at 500 °C and retentate exit pressures $P_{r.ex}$ varying from ~2 to ~20 bar. The feed stream with an $R_{S/CO}$ of 3.5 was fed at GHSV of 7500 h^{-1}. The permeate side was swept by N_2 at atmospheric pressure. The countercurrent N_2 sweep flow makes it possible to achieve a near-zero H_2 mole fraction $y_{H2,r}$ at the retentate exit (where $P_{H2,r} = y_{H2,r}P_{r,ex} \rightarrow 0$ Pa) that is required for approaching complete CO conversion for the reversible WGS reaction. These reaction conditions were chosen based on our previous experimental and modeling findings on MRs consisting zeolite membranes and doped ferrite catalysts of separation and catalytic properties comparable to this work [4,5]. The GHSV is defined by [42]

$$GHSV = \frac{\sum v_f^i}{m_{cat}/\rho_{cat}} \tag{8}$$

where v_f^i is the STP volumetric flowrate of component i (=CO, CO_2, H_2, H_2O) and m_{cat} and ρ_{cat} are the total load (g) and packing density (g/cm^3) of the catalyst, respectively. The pure N_2 sweep was maintained at a flowrate of 25 cm^3 (STP)/min. Both the retentate and permeate streams were analyzed by the online GC. The MR CO conversion χ_{CO} and H_2 recovery (R_{H2}) in permeate are defined as

$$\chi_{CO} = 1 - \frac{F_{CO}^{out}}{F_{CO}^{in}} \tag{9}$$

$$R_{H2} = \frac{Moles\ of\ H_2\ in\ permeate}{Total\ moles\ of\ H_2\ generated} \tag{10}$$

where F_{CO}^{in} and F_{CO}^{out} are the CO flowrates entering and exiting the MR, respectively, and F_{CO}^{out} accounts for CO flowrates in both retentate and permeate sides.

In the experiments of dry gas reaction on the FeCr catalyst, a conventional tubular packed bed reactor (PBR) was employed. The PBR was made of the same 10 cm long alumina tube by sealing the entire tube outer surface by the gas-impermeable glaze coating and a total amount of ~0.5 g FeCr catalyst was packed in the same way as was done in the tubular MR. However, less quartz wool was used to get a more loosely packed bed in the PBR so that that the carbon products can grow in more space without blocking the tube. While the gas products were monitored by the online GC–MS, the solid products including carbon materials and reacted catalyst particles were retrieved and examined by ex situ characterizations. The morphology and dimensions of the solid materials were observed by SEM and TEM, and their elemental compositions were examined by the EDS technique. The catalysts at different processing stages were analyzed by XPS to study the metal oxidation state changes with

reaction conditions. The XPS experiments were performed on a Thermo VG Scientific spectrometer using Al Kα (1486.7 eV) radiation as the excitation source at room temperature. The pressure of the catalyst sample chamber was maintained below 10^{-8} Pa to avoid a large amount of noise in the spectra from contaminants. The obtained binding energies were adjusted by referencing the spectra to the carbon (C 1s) peak at 284.6 eV. The MWCNTs was also characterized by Raman shift spectroscopy for assessment of the graphitic phase and crystallinity and by thermogravimetric analysis (TGA) to estimate the amount of carbon product.

4. Conclusions and Perspectives

The nanocrystalline FeCr catalyst with an atomic ratio of Fe/Cr = 10:1 was capable of coproducing H_2 and MWCNTs with near-complete CO conversion (χ_{CO} > 99.5%) by WGS reaction at 500 °C and ~20 bar in a H_2-permselective MR. The MWCNT formation in the HTP WGS MR apparently involved catalyst surface carbonizations of both CO and CH_4, with the latter being a major byproduct of WGS reaction favored at high pressures. Extended experiments on the dry gas reactions indicated synergistic effects of CO and CH_4 carbonization reactions, which promoted the rapid growth of uniform and highly crystalline MWCNTs at atmospheric pressure and 500 °C, which is a temperature much lower than those for CVD synthesis of CNTs from either CO or CH_4 on metallic nanoparticles. The MWCNTs formed from the CO/CH_4 dry mixture were of higher crystallinity and dimensional uniformity and greater length than those from the HTP WGS membrane reactions apparently because of the further reduction of Fe^{2+} to Fe^0 in the dry gas conditions that was not observed in the WGS reaction environments. The FeCr catalyst also exhibited high tolerance to H_2S impurity in the CO/CH_4 mixture feed during the CVD synthesis of MWCNTs. The good sulfur resistance of the catalyst is practically desirable for the potential utilization of biogas and coal-derived syngas for production of high-value CNTs. Further in operando reaction kinetic studies and in situ TEM and XPS observations of the catalyst and carbon structural and chemical state evolutions are needed for understanding the reaction mechanisms to guide catalyst improvement and reaction process optimization.

Supplementary Materials: The following are available online at http://www.mdpi.com/2073-4344/10/8/927/s1. Membrane fabrication method description; Figure S1: CO conversion and CH_4 content changes during the WGS reaction in the zeolite MR at 500 °C as functions of time and pressure: (a) GHSV = 15,000 h^{-1} and $R_{S/CO}$ = 3.5, (b) GHSV = 30,000 h^{-1} and $R_{S/CO}$ = 3.5, (c) GHSV = 15,000 h^{-1} and $R_{S/CO}$ = 1.5; Figure S2: SEM and TEM images of the MWCNT tips growing on catalyst nanoparticles of various sizes during HTP WGS reaction in the zeolite MR: (a) SEM image showing MWCNTs of different diameters, (b) TEM image showing catalyst particles in MWCNTs ends, (c) a growing tip on a catalyst particle of ~10 nm in size, (d)–(f) MWCNT tips on catalyst particles of different sizes and shapes; Figure S3: Results of pure CO feed reaction at 1.5 bar: (a) CO conversion as a function of time and reaction pressure, (b) and (c) the SEM and EDS results of the solid products, and (d) and (e) TEM image showing graphitic carbon coating on catalyst and Raman shift spectrum of the carbon product; Figure S4: TEM and TGA examinations of the MWCNTs produced from a gas mixture of 80 v.%CO + 20 v.%CH_4 on the FeCr nanoparticle catalyst when reacting at 500 °C and ambient pressure: (a) TEM image showing the uniformity of the long MWCNTs, (b) HR TEM image of a MWCNT tip containing a catalyst nanoparticle that appeared to be metallic Fe based on the electron diffraction pattern and EDS data, and (c) TGA/DTA results of the raw products containing MWCNTs, large catalyst particles, and supporting glass fibers; Figure S5: Results of SEM–EDS analysis for the MWCNT/catalyst product from reaction of the CO/CH_4 mixture (80%CO + 20%CH_4) containing 500 ppmv H_2S; Figure S6: (a) The SEM image of carbon product on the FeCr catalyst generated at 500 °C and 1 bar from the feed of 80%CO + 20%CH_4 with 800 ppmv H_2S, (b) Raman shift spectrum of the carbon product, and (c) results of CO chemisorption on fresh FeCr catalyst and on FeCr catalyst treated by 1000 ppmv H_2S in N_2 gas at 500 °C for 5 h; Figure S7: The EDS survey of the FeCr catalyst indicating a Fe:Cr atomic ratio of 11 ± 1.3 that agrees with the ratio in synthesis precursor (~10:1); Figure S8: The SEM images of the MFI-type zeolite membrane synthesized on the outer surface of the alumina tube: (a) fractured cross-section and (b) surface.

Author Contributions: Conceptualization, J.D.; Data curation, X.S. and A.A.; Formal analysis, D.D., N.T.A. and J.D.; Funding acquisition, J.D.; Investigation, X.S., A.A. and D.D.; Resources, V.S. and P.G.S.; Supervision, N.T.A., V.S., P.G.S. and J.D.; Validation, V.S.; Writing—original draft, X.S.; Writing—review and editing, J.D. All authors have read and agreed to the published version of the manuscript.

Funding: This research was financially supported by the Development Service Agency of Ohio through the Ohio Coal Research and Development program (Grant no. OOECDO-D-17-13) and the U.S. Department of Energy/NETL through Grant no. DE-FE0026435. The porous alumina tube supports were provided by Media and Processes Technology Inc., Pittsburgh, USA.

Conflicts of Interest: The authors declare no conflicts of interest.

References

1. Lin, Y.S. Inorganic Membranes for Process Intensification: Challenges and Perspective. *Ind. Eng. Chem. Res.* **2018**, *58*, 5787–5796. [CrossRef]
2. Damma, D.; Smirniotis, P.G. Recent advances in iron-based high-temperature water-gas shift catalysis for hydrogen production. *Curr. Opin. Chem. Eng.* **2018**, *21*, 103–110. [CrossRef]
3. Kim, S.J.; Xu, Z.; Reddy, G.K.; Dong, J.; Smirniotis, P. Effect of Pressure on High Temperature Water Gas Shift Reaction in Microporous Zeolite Membrane Reactor. *Ind. Eng. Chem. Res.* **2012**, *51*, 1364–1375. [CrossRef]
4. Kim, S.J.; Yang, S.; Reddy, G.K.; Dong, J.; Smirniotis, P. Zeolite membrane reactor for high temperature water gas shift reaction: Experimental and simulation studies. *Energy Fuels* **2013**, *27*, 4471–4480. [CrossRef]
5. Arvanitis, A.; Sun, X.; Yang, S.; Damma, D.; Smirniotis, P.; Dong, J. Approaching Complete CO Conversion and Total H_2 Recovery for Water Gas Shift Reaction in a High-Temperature and High-Pressure Zeolite Membrane Reactor. *J. Membr. Sci.* **2018**, *549*, 575–580. [CrossRef]
6. LeValley, T.L.; Richard, A.R.; Fan, M. The progress in water gas shift and steam reforming hydrogen production technologies—A review. *Int. J. Hydrog. Energy* **2014**, *39*, 16983–17000. [CrossRef]
7. Nikolaev, P.; Bronikowski, M.J.; Bradley, R.K.; Rohmund, F.; Colbert, D.T.; Smith, K.A.; Smalley, R.E. Gas-phase catalytic growth of single-walled carbon nanotubes from carbon monoxide. *Chem. Phys. Lett.* **1999**, *313*, 91–97. [CrossRef]
8. Selbmann, D.; Bendjemil, B.; Leonhardt, A.; Pichler, T.; Täschner, C.; Ritschel, M. A parametric study of the synthesis and purification of single-walled carbon nanotubes using the high-pressure carbon monoxide process. *Appl. Phys. A* **2008**, *90*, 637–643. [CrossRef]
9. Ashik, U.P.M.; Daud, W.W.; Abbas, H.F. Production of greenhouse gas free hydrogen by thermocatalytic decomposition of methane—A review. *Renew. Sustain. Energy Rev.* **2015**, *44*, 221–256. [CrossRef]
10. Tang, L.; Yamaguchi, D.; Burke, N.; Trimm, D.; Chiang, K. Methane decomposition over ceria modified iron catalysts. *Catal. Commun.* **2010**, *11*, 1215–1219. [CrossRef]
11. Gunugunuri, K.R.; Kim, S.J.; Dong, J.; Jasinski, J.B.; Smirniotis, P. Long-term WGS stability of Fe/Ce and Fe/Ce/Cr catalysts at high and low steam to CO ratios—XPS and Mössbauer spectroscopic study. *Appl. Catal. A Gen.* **2012**, *415*, 101–110.
12. Lee, S.H.; Park, J.P.; Kim, H.R.; Lee, J.G.; Hong, K.H. Synthesis of high-quality carbon nanotube fibers by controlling the effects of sulfur on the catalyst agglomeration during the direct spinning process. *RSC Adv.* **2015**, *5*, 41894–41900. [CrossRef]
13. Moon, S.Y.; Kang, I.J.; Kim, S.M.; Kim, W.S. Influence of the Sulfur Content Catalyst on the Packing Density of Carbon Nanotube Forests. *Nanomaterials* **2019**, *9*, 889. [CrossRef]
14. Wang, H.; Wei, L.; Ren, F.; Wang, Q.; Pfefferle, L.D.; Haller, G.L.; Chen, Y. Chiral-Selective $CoSO_4/SiO_2$ Catalyst for Single-Walled Carbon Nanotube Growth. *ACS Nano* **2013**, *7*, 614–626. [CrossRef]
15. Wang, H.; Ren, F.; Liu, C.; Si, R.; Yu, D.; Pfefferle, L.D.; Haller, G.L.; Chen, Y. $CoSO_4/SiO_2$ catalyst for selective synthesis of single-walled carbon nanotubes: Effect of catalyst calcination. *J. Catal.* **2013**, *300*, 91–101. [CrossRef]
16. Wang, H.; Yang, L.; Sui, X.; Karhan, H.E.; Wang, X.; Chen, Y. Selective synthesis of single walled carbon nanotubes on metal (iron, nickel or cobalt) sulfate-based catalysts. *Carbon* **2018**, *129*, 128–136. [CrossRef]
17. Rhodes, C.; Williams, P.B.; King, F.; Hutchings, G.J. Promotion of Fe_3O_4/Cr_2O_3 high temperature water gas shift catalyst. *Catal. Commun.* **2002**, *3*, 381–384. [CrossRef]
18. Damma, D.; Smirniotis, P.G. Effects of the Ce and Cr Contents in Fe−Ce−Cr Ferrite Spinels on the High-Temperature Water—Gas Shift Reaction. *Ind. Eng. Chem. Res.* **2017**, *56*, 1772–1781.
19. Choudhary, T.V.; Aksoylu, E.; Goodman, D.W. Nonoxidative Activation of Methane. *Catal. Rev.* **2003**, *45*, 151–203. [CrossRef]
20. Gu, X.; Zhang, J.; Dong, J.; Nenoff, T.M. A Platinum-Cobalt-Loaded NaY Zeolite Membrane for Nonoxidative Conversion of Methane to Higher Hydrocarbons and Hydrogen. *Catal. Lett.* **2005**, *102*, 9–13. [CrossRef]
21. Robertson, J. Heterogeneous catalysis model of growth mechanisms of carbon nanotubes, graphene and silicon nanowires. *J. Mater. Chem.* **2012**, *22*, 19858–19862. [CrossRef]

22. Hofmann, S.; Sharma, R.; Ducati, C.; Du, G.; Mattevi, C.; Cepek, C.; Cantoro, M.; Pisana, S.; Parvez, A.; Cervantes-Sodi, F.; et al. In situ Observations of Catalyst Dynamics during Surface-Bound Carbon Nanotube Nucleation. *Nano Lett.* **2007**, *7*, 602–608. [CrossRef] [PubMed]
23. Rönsch, S.; Schneider, J.; Matthischke, S.; Schlüter, M.; Götz, M.; Lefebvre, J.; Prabhakaran, P.; Bajohr, S. Review on methanation—From fundamentals to current projects. *Fuel* **2016**, *166*, 276–296. [CrossRef]
24. Chen, C.J.; Back, M.H.; Back, B.A. The Thermal Decomposition of Methane. I. Kinetics of the Primary Decomposition to C_2H_6+H_2; Rate Constant for the Homogeneous Unimolecular Dissociation of Methane and its Pressure Dependence. *Can. J. Chem.* **1975**, *53*, 3580–3590. [CrossRef]
25. Pinilla, J.L.; Utrilla, R.; Lázaro, M.J.; Moliner, R.; Suelves, I.; García, A.B. Ni- and Fe-based catalysts for hydrogen and carbon nanofilament production by catalytic decomposition of methane in a rotary bed reactor. *Fuel Process. Technol.* **2011**, *92*, 1480–1488. [CrossRef]
26. Moothi, K.; Simate, G.S.; Falcon, R.; Iyuke, S.E.; Meyyappan, M. Carbon Nanotube Synthesis Using Coal Pyrolysis. *Langmuir* **2015**, *31*, 9464–9472. [CrossRef]
27. Jia, Z.; Kou, K.; Qin, M.; Wu, H.; Puleo, F.; Liotta, L.F. Controllable and Large-Scale Synthesis of Carbon Nanostructures: A Review on Bamboo-Like Nanotubes. *Catalysts* **2017**, *7*, 256. [CrossRef]
28. Shandakov, S.D.; Kosobutsky, A.V.; Rybakov, M.S.; Sevostyanov, O.G.; Russakov, D.M.; Lomakin, M.V.; Vershinina, A.I.; Chirkova, I.M. Effect of gaseous and condensate products of ethanol decomposition on aerosol CVD synthesis of single-walled carbon nanotubes. *Carbon* **2018**, *126*, 522–531. [CrossRef]
29. Gili, A.; Schlicker, L.; Bekheet, M.F.; Görke, O.; Penner, S.; Grünbacher, M.; Götsch, T.; Littlewood, P.; Marks, T.J.; Stair, P.C.; et al. Surface Carbon as a Reactive Intermediate in Dry Reforming of Methane to Syngas on a 5% Ni/MnO Catalyst. *ACS Catal.* **2018**, *8*, 8739–8750. [CrossRef]
30. Anoshkin, I.V.; Nasibulin, A.G.; Tian, Y.; Liu, B.; Jiang, H.; Kauppinen, E.I. Hybrid carbon source for single-walled carbon nanotube synthesis by aerosol CVD method. *Carbon* **2014**, *78*, 130–136. [CrossRef]
31. Hata, K.; Futaba, D.N.; Mizuno, K.; Namai, T.; Yumura, M.; Iijima, S. Water-Assisted Highly Efficient Synthesis of Impurity-Free Single-Walled Carbon Nanotubes. *Science* **2004**, *306*, 1362–1364. [CrossRef] [PubMed]
32. Pumera, M.; Iwai, H. Multicomponent Metallic Impurities and Their Influence upon the Electrochemistry of Carbon Nanotubes. *J. Phys. Chem. C* **2009**, *113*, 4401–4405. [CrossRef]
33. Srikanth, I.; Padmavathi, N.; Prasad, P.S.R.; Ghosal, P.; Jaini, R.K.; Subrahmanya, C. Effect of high-temperature heat treatment duration on the purity and microstructure of MWCNTs. *Bull. Mater. Sci.* **2016**, *39*, 41–46. [CrossRef]
34. Zhang, B.; Piao, G.; Zhang, J.; Bub, C.; Xie, H.; Wu, B.; Kobayashi, N. Synthesis of carbon nanotubes from conventional biomass-based gasification Gas. *Fuel Process. Technol.* **2018**, *180*, 105–113. [CrossRef]
35. Kuznetsov, B.N.; Chudinov, M.G.; Alekseev, A.M.; Yakerson, V.I. Effect of reaction mixture, oxidative and reductive media on element distribution and iron valence state on the surface of a medium-temperature iron-chromium catalyst. *Kinet. Catal.* **1996**, *37*, 846–849.
36. Furlan, A.; Jansson, U.; Lu, J.; Hultman, L.; Magnuson, M. Structure and bonding in amorphous iron carbide thin films. *J. Phys. Condens. Matter* **2015**, *27*, 045002. [CrossRef]
37. Da Cunha, T.H.R.; De Oliveira, S.; Martins, I.L.; Geraldo, V.; Miquita, D.; Ramos, S.L.M.; Lacerda, R.G.; Ladeira, L.O. High-yield synthesis of bundles of double- and triple-walled carbon nanotubes on aluminum flakes. *Carbon* **2018**, *133*, 53–61. [CrossRef]
38. Gu, X.; Tang, Z.; Dong, J. On-Stream Modification of MFI Zeolite Membranes for Enhancing Hydrogen Separation at High Temperature. *Microporous Mesoporous Mater.* **2008**, *111*, 441–448. [CrossRef]
39. Tang, Z.; Nenoff, T.M.; Dong, J. Internal Surface Modification of MFI-Type Zeolite Membranes for High Selectivity and High Flux for Hydrogen. *Langmuir* **2009**, *25*, 4848–4852. [CrossRef]
40. Masuda, T.; Fukumoto, N.; Kitamura, M. Modification of pore size of MFI-type zeolite by catalytic cracking of silane and application to preparation of H_2-separating zeolite membrane. *Microporous Mesoporous Mater.* **2001**, *48*, 239–245. [CrossRef]
41. Palma, V.; Ruocco, C.; Cortese, M.; Martino, M. Recent Advances in Structured Catalysts Preparation and Use in Water-Gas Shift Reaction. *Catalysts* **2019**, *9*, 991. [CrossRef]
42. Haber, J. Manual on Catalyst Characterization. *Pure Appl. Chem.* **1991**, *63*, 1227–1246. [CrossRef]